Journal of Materials Chemistry A

Photoinduced electron doping of single-walled carbon nanotubes based on carboxamide photochemical reactions

Journal:	*Journal of Materials Chemistry A*
Manuscript ID	TA-ART-10-2022-008131.R2
Article Type:	Paper
Date Submitted by the Author:	27-Jan-2023
Complete List of Authors:	Tanaka, Naoki; Kyushu University, Applied Chemistry Ishii, Taiki; Kyushu University Hamasuna, Aoi; Kyushu University Yamaguchi, Itsuki; Kyushu University Fujigaya, Tsuyohiko; Kyushu Daigaku Kogakubu Daigakuin Kogakufu,

PAPER

Photoinduced electron doping of single-walled carbon nanotubes based on carboxamide photochemical reactions

aaReceived 00th January 20xx,
Accepted 00th January 20xx

DOI: 10.1039/x0xx00000x

Naoki Tanaka,[ab] Taiki Ishii,[a] Itsuki Yamaguchi,[a] Aoi Hamasuna,[a] and Tsuyohiko Fujigaya*[abc]

1,3-Dimethyl-2-arylbenzimidazole (DMBI) derivatives act as good electron dopants for semiconductors and form DMBI cations (DMBI$^+$). However, in the presence of oxygen, inactive oxygen adducts (DMBI-Ox) are produced by the reaction of DMBI radicals with oxygen molecules, which decreases the doping efficiency. In this study, we found that UV irradiation of DMBI-Ox generates DMBI$^+$ and hydroxyl ions that act as electron dopants. The underlying mechanism is likely the intramolecular cyclization of DMBI-Ox, followed by the elimination of hydroxyl ions. As an application of the new photoinduced reaction of DMBI-Ox, we carried out photoinduced electron doping of single-walled carbon nanotubes (SWCNTs) using DMBI-Ox to convert p-type SWCNTs into n-type SWCNTs. The photochemical reaction proceeded on the surface of the SWCNTs in the solid state, and the photodoped n-type SWCNTs showed air stability for 20 days owing to the generation of chemically stable DMBI$^+$ on the negatively charged SWCNT surface. This doping method offers a facile preparation method for SWCNT sheets with a p–n pattern using photomasks. We fabricated planar-type thermoelectric generator (TEG) devices using p–n-patterned SWCNT sheets. The TEG device with four p–n sequences on a hot plate (ΔT = 35 °C) showed open-circuit voltage and maximum power density values of 0.68 mV and 0.504 nW, respectively. We believe that this new photochemical n-doping method will offer various applications based on the fine and facile patterning capabilities of these sheets.

1. Introduction

Based on the Peltier effect and Seebeck effect, the thermoelectric conversion that mutually converts electricity and heat is an essential technology in electronic devices such as cooling systems,[1] independent power supplies,[2] and sensors.[3] Especially with the recent proliferation of IoT devices, compact and high-performance thermoelectric generators (TEG) are increasingly required.[4] Generally, TEGs consist of P-type and N-type semiconductors using organic and inorganic materials connected in series alternately using metal or conductive paste. To enhance their performance, a large power factor (PF = $S^2\sigma$), which is composed of Seebeck coefficient (S) and electrical conductivity (σ), respectively, is preferable.

Among them, chemical doping using electron donor and acceptor molecules is crucial for controlling the frontier orbital energy gap. 1,3-Dimethyl-2-arylbenzimidazole (DMBI) derivatives are excellent electron dopants (n-dopants) for organic semiconductors[5-14] and nanocarbons, such as fullerene,[15-18] graphene,[19-22] and single-walled carbon nanotubes (SWCNTs).[23-26] During doping, DMBI radicals (DMBI$^\bullet$) or DMBI cations (DMBI$^+$) are generated by the homolytic or heterolytic dissociation of the C–H bond in DMBI, respectively, and the generated radicals or hydride (H^-) have been proposed for use as electron donors to semiconductors. Generally, n-doping by DMBI derivatives is carried out using a solution of DMBI derivatives through the dipping of semiconductors or drop-casting of dopant solutions onto semiconductors.[1-22] However, the excessively high reactivity of these species, especially for DMBI$^\bullet$, often leads to side reactions, such as dimerization and oxidation reactions.[27]

The side product DMBI-Ox was reported to be formed by the reaction of DMBI$^\bullet$ with molecular oxygen.[27,28] Recently, Bardagot and co-workers demonstrated that UV irradiation (λ_{ex} = 315–435 nm) of *p*-NMe_2-DMBI (N-DMBI) generates N-DMBI-Ox as an inactive oxygen adduct in apolar solvents, such as toluene and chlorobenzene at room temperature, whereas it generates N-DMBI$^+$ in polar solvents (Fig. 1a).[28] They reported that the generation of N-DMBI-Ox decreased the doping efficiency of N-DMBI, which was likely due to the consumption of N-DMBI$^\bullet$ for the reaction with oxygen molecules.[28] Therefore, dark conditions using degassed solvents are required to avoid the generation of N-DMBI-Ox and maximize the doping efficiency.

In this study, we discovered a new photochemical reaction of DMBI-Ox triggered by UV irradiation and identified a method of utilizing DMBI-Ox as a photoinduced electron dopant based on this reaction. *o*-Phenylenediamine derivatives are benzimidazole precursors,[25-31] and benzimidazole rings are

[a] *Department of Applied Chemistry, Graduate School of Engineering, Kyushu University, 744 Motooka, Nishi-ku, Fukuoka 819-0395, Japan. E-mail: fujigaya.tsuyohiko.948@m.kyushu-u.ac.jp*
[b] *International Institute for Carbon Neutral Energy Research (WPI-I2CNER), 744 Motooka, Nishi-ku, Fukuoka 819-0395, Japan*
[c] *Center for Molecular Systems (CMS), 744 Motooka, Nishi-ku, Fukuoka 819-0395, Japan*
† Electronic Supplementary Information (ESI) available: Additional spectroscopic data, Seebeck coefficient data. See DOI: 10.1039/x0xx00000x

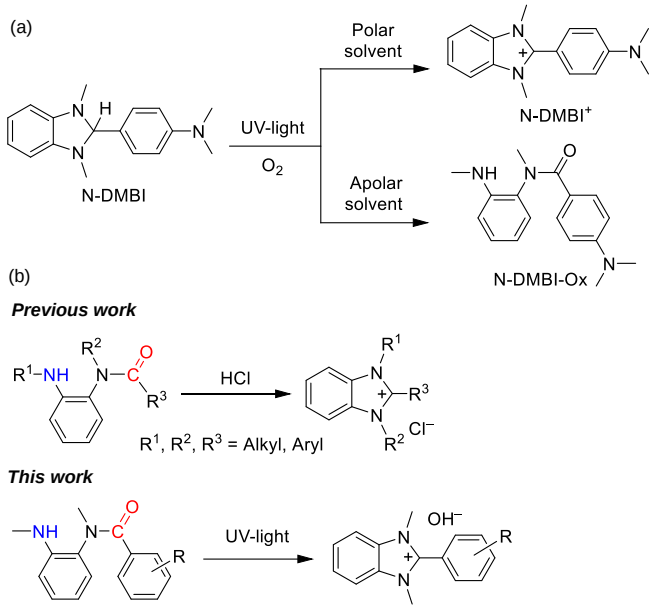

Fig. 1 (a) Photochemical reactions of N-DMBI by UV irradiation in polar and apolar solvents containing oxygen. (b) Intramolecular cyclization reaction of DMBI-Ox derivatives by acid condition (previous work) and UV irradiation (this work).

generally synthesized by intermolecular coupling of *o*-phenylenediamine derivatives with oxides, such as carboxylic acids, nitriles, and aldehydes, with C–N bond formation.[29-34] In contrast, DMBI-Ox can be formed by intramolecular cyclization reactions because of the hydrogen atom of the secondary amine and the amide group as an oxidant. In fact, Diver and co-workers successfully synthesized benzimidazolium salts with various substituents at the C-2 position using *N*,*N*′-trisubstituted benzimidazole derivatives under acidic conditions;[35] however, the photochemical reaction of DMBI-Ox has never been demonstrated (Fig. 1b). Considering the presence of a δ-hydrogen in the amide, UV irradiation of DMBI-Ox was expected to cause a Norrish type II reaction.[36-43] As a result of the photochemical reaction of DMBI-Ox with UV light, $DMBI^+$ and hydroxyl ions (OH^-) are generated via the intramolecular cyclization of DMBI-Ox. We investigated the photochemical reactions of DMBI-Ox, both in solution and in the solid state. As an application for doping, we demonstrated photoinduced n-doping of SWCNTs based on the photochemical reaction of DMBI-Ox. Finally, we fabricated an SWCNT sheet patterned into p- and n-type regions using a photomask and developed thermoelectric devices based on the SWCNTs.

2. Experimental section

2.1 Materials

N-DMBI and NO_2-DMBI were synthesized according to the literature.[44] SWCNTs (Meijo-eDIPS) with a diameter of 1.5 ± 0.5 nm were purchased from Meijo Nano Carbon. Ethanol, hexane, and *N*-methylpyrrolidone (NMP) were purchased from FUJIFILM Wako Pure Chemicals Corp (Tokyo, Japan). Ethanol (EtOH), dimethyl sulfoxide (DMSO), dichloromethane (CH_2Cl_2), tetrahydrofuran (THF), and hexane (Hexane) were purchased from DOJINDO Corp. (Kumamoto, Japan). Silica aerogel (ENOVA, IC3110) and poly(vinyl alcohol) were purchased from Cabot Corp (Boston, USA) and MilliporeSigma (St. Louis, USA), respectively.

2.2 Characterization

^1H and ^{13}C NMR spectra were recorded using a JEOL JNM-ECZ400 (400 MHz). Electrospray ionization mass spectroscopy was conducted using an AccuTOF LC-plus 4G system (JEOL, Tokyo Japan). UV-vis absorption measurements were performed using a V-670 spectrophotometer (JASCO, Tokyo Japan). X-ray photoelectron spectroscopy was conducted at room temperature using an AXIS-ULTRA spectrometer (Shimadzu, Kyoto Japan), in which indium was used as the substrate. The in-plane electrical conductivity and in-plane Seebeck coefficient were measured using a ZEM-3 measurement system (ADVANCE RIKO, Yokohama Japan) under a helium atmosphere at ~0.01 MPa from 30 °C. The *I–V* performance was measured using a Keithley 2401 source meter (Tektronix, Tokyo Japan). 254-nm and 365-nm UV light were provided using a tabletop UV lamp (AS ONE, Osaka, Japan) and LED handy light (OptoCode, Tokyo, Japan), which the light intensities from a distance of 1 cm from the specimen were 3.5 mW/cm^2 and 50.0 mW/cm^2, respectively.

2.3 Synthesis of N-DMBI-Ox

Under oxygen, a dry hexane solution of N-DMBI (1.00 g, 3.74 mmol) was stirred for 12 h at 50 °C. After thermal filtration at 70 °C, the filtrate was cooled to 0 °C to give N-DMBI-Ox as a brown powder (689 mg, 2.43 mmol) in 65% yield: ^1H NMR (400 MHz, $CDCl_3$): δ (ppm) 7.26 (d, J =8.7 Hz, 2H), 7.14 (dd, J = 8.7, 8.5 Hz, 1H), 6.76 (d, J = 7.3 Hz, 1H), 6.67 (d, J = 8.2 Hz, 1H), 6.52 (dd, J = 7.8, 7.8 Hz, 1H), 6.40 (d, J = 8.7 Hz, 2H), 4.20 (s, 1H), 3.24 (s, 3H), 2.94 (d, J = 5.5 Hz, 3H), 2.90 (s, 6H). ^{13}C NMR (100 MHz, $CDCl_3$): δ (ppm) 171.9, 151.5, 144.6, 131.6, 130.3, 128.6, 121.9, 117.1, 110.7, 110.5, 40.1, 36.9, 30.4. ESI-TOF MS: calcd. for C17H21N3 [M]+: *m/z* = 267.17; found: 267.17.

2.4 Synthesis of NO_2-DMBI-Ox

Under oxygen, a dry hexane solution of NO_2-DMBI (1.00 g, 3.71 mmol) was stirred for 12 h at 50 °C. After thermal filtration at 70 °C, the filtrate was recrystallized at 0 °C to give NO_2-DMBI-Ox as yellow crystals (869 mg, 3.04 mmol) in 82% yield: ^1H NMR (400 MHz, $CDCl_3$): δ (ppm) 8.17 (s, 1H), 8.06 (d, J =8.2 Hz, 1H), 7.68 (d, J = 6.9 Hz, 1H), 7.34 (dd, J = 8.2, 8.2 Hz, 1H), 7.11 (dd, J = 7.8, 7.8 Hz, 1H), 6.72 (d, J = 7.8 Hz, 1H), 6.64 (d, J = 8.2 Hz, 1H), 6.48 (dd, J = 7.8, 7.8 Hz, 1H), 4.23 (s, 1H), 3.34 (s, 3H), 2.98 (d, J = 5.0 Hz, 3H). ^{13}C NMR (100 MHz, $CDCl_3$): δ (ppm) 169.7, 147.5, 144.7, 137.2, 133.7, 129.9, 129.2, 129.0, 128.6, 124.7, 123.0, 117.2, 111.3, 36.5, 30.3. ESI-TOF MS: calcd. for C15H14N303 [M]+: m/z = 285.30; found: 285.30.

2.5 Preparation of SWCNT on PTFE membrane

SWCNTs (1.0 mg) were suspended in NMP (30 mL) using a bath-type sonicator for 1 hour and a tip-type sonicator for 1 hour. The dispersion was centrifuged at 12700 rpm for 30 min, and

the supernatant (ca. top 90%) was collected as the solution of SWCNTs. The solution was diluted with NMP to prepare a 50 mL NMP solution. The SWCNT solution (10 mL) was filtered through a PTFE membrane (diameter: 47 mm) to obtain SWCNT sheets of 1 to 3 μm thickness on PTFE. Three SWCNT sheets were prepared from the different batches of the pristine SWCNTs. SWCNT sheets were used without peeling off from the PTFE membrane to support the thin SWCNT sheets.

2.6 Photoinduced electron doping of SWCNT based on a photochemical reaction of NO_2-DMBI-Ox

The SWCNT sheets on a PTFE membrane were cut into 14 mm × 4 mm pieces, and the sheets were dipped into a 1.0 mM ethanol solution of NO_2-DMBI-Ox for 10 minutes. The SWCNT sheets after dipping were dried in a vacuum at room temperature for 8 hours. The obtained SWCNT sheets were irradiated using a 365-nm UV light and then evaluated for thermoelectric properties.

2.7 Fabrication of planar SWCNT-based TEGs

Cu wire (diameter: 1.0 mm) was attached at the boundary between the p- and n-doped regions on one side of the SWCNT sheet on the PTFE membrane. The other areas of the sheet surface were passivated using a silica aerogel/poly(vinyl alcohol) composite insulator. Au wire was connected to both ends of the SWCNT sheet using Ag paste.

3. Results and discussion

3.1 Photochemical reaction of DMBI-Ox

DMBI-Ox was synthesized by heating a hexane solution of DMBI at 50 °C under oxygen atmosphere (Fig. 2a). In this study, N-DMBI-Ox and DMBI-Ox containing a nitro group at the *meta*-position (NO_2-DMBI-Ox) were synthesized (Fig. 2a). The absorption spectrum of N-DMBI-Ox showed a broad absorption band in the UV region in ethanol (EtOH), and the maximum absorption wavelength was 306 nm. An N-DMBI-Ox solution in EtOH (0.02 mM) was irradiated by UV light (λ_{ex} = 254 nm). As shown in Fig. 2b, a characteristic absorption peak at 306 nm was decreased and a new absorption peak centered at 342 nm appeared after UV irradiation, and the maximum intensity at 342 nm was reached after 110 min (Fig. S1†). The UV-vis spectrum of the solution after UV irradiation was consistent with that of N-DMBI$^+$I$^-$ in EtOH (Fig. 2c). The observation of isosbestic points at 250 nm, 272 nm, and 320 nm clearly indicates that the photochemical reaction proceeded without forming side products. Interestingly, the photochemical reaction of N-DMBI-Ox only occurred in polar solvents, such as EtOH and DMSO, whereas the peaks were decreased after irradiation in apolar solvents, such as hexane, THF, and CH_2Cl_2, which was likely due to the photoinduced decomposition of the compounds (Fig. S2†). On the other hand, for NO_2-DMBI-Ox, irradiation at 254 nm in EtOH produced a new broad absorption band centered at 280 nm and the maximum intensity was reached after 30 min (Fig. S3†). This peak was consistent with that of NO_2-DMBI$^+$I$^-$ (Fig. S4†), although it did not show the isosbestic points during the photochemical reaction, thus indicating the formation of side products. We considered that the photolysis reaction of nitrophenyl compounds that occurred after UV light application and the generated nitric oxide and oxygen radical adducts led to the generation of side products.[45,46]

To identify the products after irradiation, ^{1}H NMR measurements of N-DMBI-Ox were performed before and after 254-nm irradiation for 72 h using 0.04 mM deuterated EtOH solutions (Fig. 2d). In the ^{1}H NMR spectrum, the aromatic protons at 7.26, 7.12, 6.70, 6.66, and 6.45 ppm were almost diminished; new peaks at 8.01, 7.76, 7.71, and 7.06 ppm were observed at a lower magnetic field after irradiation, and aliphatic protons at 3.20 ppm and 4.05 ppm with an integration ratio of 1:2 were observed (red line in Fig. 2d). We recognized that the spectrum after irradiation is consistent with that of N-

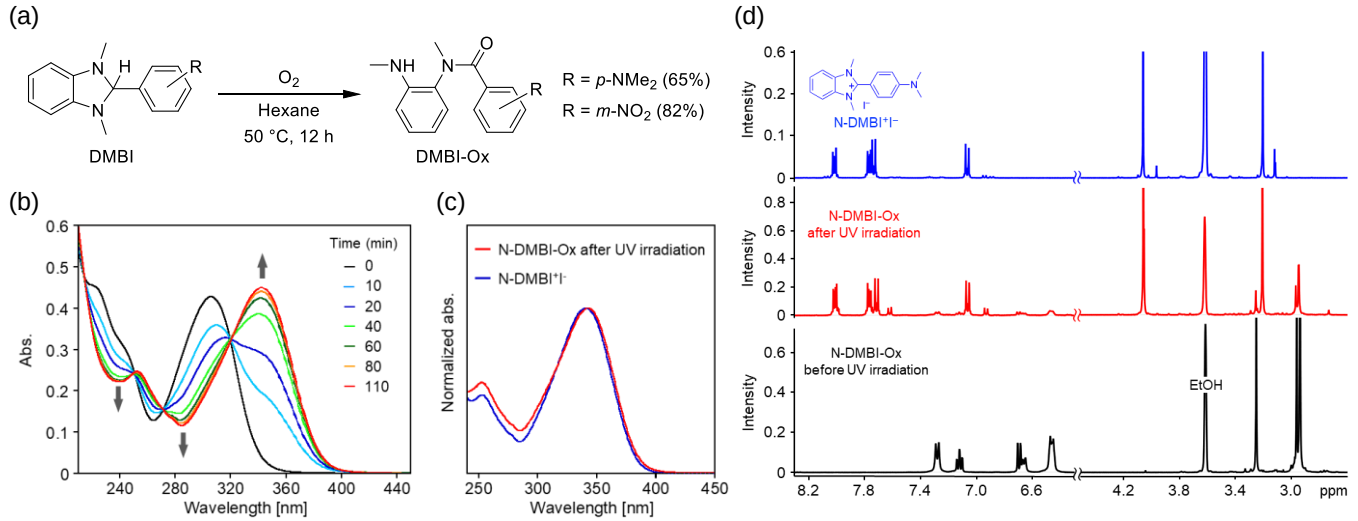

Fig. 2 (a) Synthesis of DMBI-Ox from DMBI derivatives. (b) UV-vis absorption spectra of N-DMBI-Ox in EtOH (0.02 mM) upon UV irradiation at 254 nm. (c) UV-vis absorption spectra of N-DMBI-Ox after UV irradiation (red) and N-DMBI$^+$I$^-$ in EtOH (blue). (d) ^{1}H NMR spectra of N-DMBI$^+$I$^-$ (blue) and N-DMBI-Ox before (black) and after (red) UV irradiation for 72 hours in EtOH-d_3 solution.

$DMBI^+I^-$ (blue line in Fig. 2d) and concluded that the UV irradiation of N-DMBI-Ox generates N-$DMBI^+$. On the other hand, the ^1H NMR spectrum of the deuterium EtOH solution of NO_2-DMBI-Ox after irradiation at 254 nm for 72 h also showed a decrease in the peak intensity of NO_2-DMBI-Ox and the appearance of new peaks in the aromatic region, with peak patterns consistent with NO_2-$DMBI^+I^-$ (blue line in Fig. S5†). The presence of several peaks not assignable to NO_2-$DMBI^+I^-$ was based on the compounds formed by photolysis of the nitrophenyl group.[45,46]

3.2 Photochemical Reaction Mechanism of DMBI-Ox

A possible mechanism for the photochemical reaction of DMBI-Ox is as follows: DMBI-Ox undergoes intramolecular cyclization via δ-hydrogen transfer (Norrish type II reaction) under UV irradiation, which gives rise to DMBI-OH as a reaction intermediate (Scheme 1). Subsequently, $DMBI^+$ is generated as a result of the elimination of a hydroxyl ion as the counter anion (Pathway I in Scheme 1). The stabilization of $DMBI^+$ and hydroxyl ions by the solvation of polar solvents was considered the reason for the heterolytic dissociation of C–O of DMBI-OH in EtOH, whereas unstable DMBI radical preferentially formed in apolar solvents is considered the reason for the observed decomposition (Pathway II in Scheme 1, Fig. S2†). To confirm the generation of hydroxyl ions in the photochemical reaction of DMBI-Ox, we checked the pH of the N-DMBI-Ox suspension in H_2O before and after irradiation with 254-nm UV light for 30 min. The pH of the solution increased from 9.01 to 9.61, indicating the generation of hydroxyl ions. In addition, the UV-vis spectroscopy confirmed the formation of N-$DMBI^+$ (Fig. S6†). Because hydroxyl ions and $DMBI^•$ produced by UV irradiation are known as electron dopants,[47,48] our findings suggest that DMBI-Ox can be used as a dopant for semiconductors by UV irradiation.

3.3 Photoinduced Electron Doping of SWCNTs

As an application of the new photoinduced reaction of DMBI-Ox, we performed electron doping of SWCNTs using DMBI-Ox. Because the as-prepared SWCNTs are p-type in nature due to oxidation by air, the electron doping of SWCNTs using an n-dopant is necessary to utilize them as a component of semiconductor devices based on p-type and n-type SWCNTs, such as field effect transistor and thermoelectric devices.[24,49,50] In this study, SWCNT sheets (pristine SWCNT; approximately 3 μm in thickness) were prepared on the polytetrafluoroethylene (PTFE) membrane by filtering SWCNT dispersions in *N*-methylpyrrolidone (NMP), and the doping nature was investigated by evaluating the Seebeck coefficient and electrical conductivity of the sheets doped with DMBI-Ox (doped-SWCNT sheets) before and after the UV irradiation (Fig. 3a).

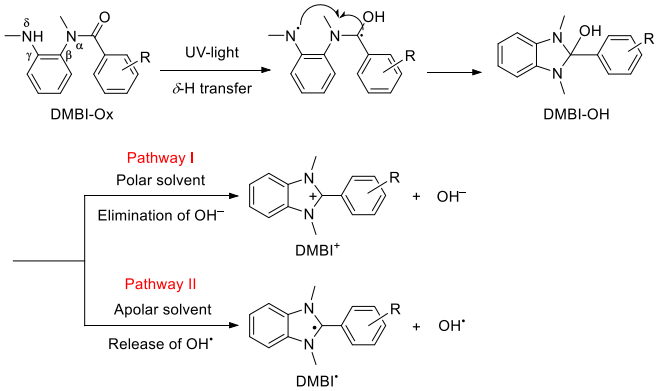

Scheme 1 Plausible mechanism of photochemical reaction of DMBI-Ox by UV irradiation.

In Fig. 3b and 3c, the Seebeck coefficient and electrical conductivity of the SWCNT sheets before and after UV irradiation are plotted, respectively. The Seebeck coefficient of pristine SWCNT sheets was 44.0 μVK^{-1}, indicating the p-type nature of the sheets (black plot in Fig. 3b). Relatively low electrical conductivity of the SWCNT sheets (~7.78×10^3 Sm^{-1}, Fig. 3c) compared to the other reports using the same SWCNT source[24-26] might be due to the harsh sonication by tip-sonicator that was applied to sufficiently unravel SWCNT bundles to increase doping efficiency.[52] After the dipping of the SWCNT sheets for 10 min in the 1.0 mM EtOH solution of N-DMBI-Ox at 30 °C, the Seebeck coefficient of the sheet shifted to 7.52 μVK^{-1} (green plot in Fig. 3b), while after dipping in the 1.0 mM EtOH solution of NO_2-DMBI-Ox at 30 °C, such a significant change was not observed, and the value only shifted to 38.6 μVK^{-1} (red plot at 0 min in Fig. 3b). Therefore, we used NO_2-DMBI-Ox for further experiments. Note that doping in the 2.0 mM EtOH solution of NO_2-DMBI-Ox produced a Seebeck coefficient of 0.99 μVK^{-1} without UV irradiation (blue plot in Fig. 3b). This decrease in the Seebeck coefficient was attributed to an electron donation from amide N in NO_2-DMBI-Ox.

For the photochemical reaction on SWCNT sheets, 365-nm UV light was used instead of 254-nm light because 1) oxidation of the SWCNT sidewalls by 254-nm irradiation has been reported[51] and 2) strong photoabsorption of the SWCNTs by 254-nm irradiation can be avoided. After irradiation of the SWCNT sheet for 20 min, the Seebeck coefficient of the SWCNT sheet became negative and shifted to –39.3 μVK^{-1}. In addition, the electrical conductivity of the SWCNT sheet increased from 4.23×10^3 Sm^{-1} to 5.41×10^3 Sm^{-1} after irradiation (Fig. 3c). These results clearly indicate that NO_2-DMBI-Ox can act as a photoinduced electron dopant for the SWCNTs in the solid state. Although Seebeck coefficient and electrical conductivity generally have a trade-off relationship, the change of the Seebeck coefficient upon UV light irradiation from 0 to 10 min did not lead to a significant change in electrical conductivity. We attribute such a trend to the presence of the metallic SWCNTs in the sheets as we evidenced by comparing between semiconducting SWCNT sheets and SWCNT sheets containing both metallic and semiconducting SWCNTs.[52] We found that irradiation over 1 h resulted in a decrease in the absolute Seebeck coefficient, indicating the oxidation of the doped sheets under irradiation.

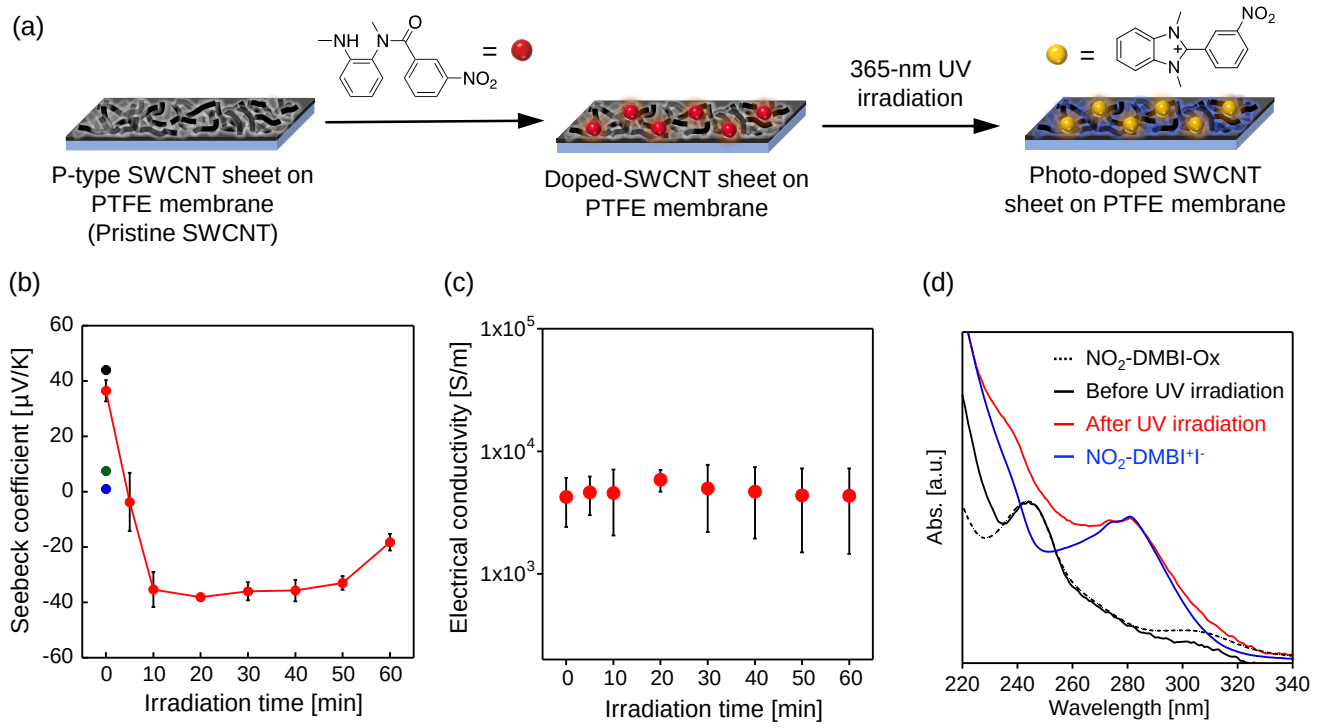

Fig. 3 (a) Photoinduced doping of SWCNT sheets using DMBI-Ox. (b) Irradiation time dependency of the Seebeck coefficient of the SWCNT sheets dipped in the 1.0 mM NO_2-DMBI-Ox solution (red line). Seebeck coefficient of the pristine SWCNT sheet (black) and SWCNTs dipped in the 1.0 mM N-DMBI-Ox solution (green) and 2.0 mM NO_2-DMBI-Ox solution (blue) were also plotted. (c) Irradiation time dependency of the electrical conductivity of the SWCNT sheet dipped in 1.0 mM NO_2-DMBI-Ox solutions. Error bars represent the standard deviation of technical replicates. (d) UV-vis absorption spectra of NO_2-$DMBI^+I^-$ (blue solid line) and NO_2-DMBI-Ox (black dotted line) extracted products from SWCNT sheets before (dark solid line) and after (red solid line) photoinduced doping.

To characterize the chemical structure of the dopants on the SWCNTs, the doped-SWCNT sheets before and after UV irradiation were dipped into EtOH to extract the dopants on the sheet, and then the UV-vis spectra of the extracted solutions were measured (Fig. 3d). The absorption spectrum of the solution extracted from the doped-SWCNT sheet before irradiation (black solid line) is consistent with that of NO_2-DMBI-Ox, while that of the solution extracted from doped-SWCNT sheet after irradiation (red line) shows a peak centered at 280 nm, which is consistent with the peaks of NO_2-$DMBI^+$ (blue line), indicating that the photochemical reaction proceeded on the SWCNTs in the solid state. We speculated that the generation of NO_2-$DMBI^+$ accompanied by electron doping on the SWCNT surface was facilitated even in the absence of solvent, which was likely due to the presence of an electron acceptor (i.e., SWCNTs). Noted that the progress of the photochemical reaction of DMBI-Ox in the solid state was also confirmed by the diffuse reflectance spectra of N-DMBI-Ox and NO_2-DMBI-Ox (Fig. S7†). We also measured the UV absorption spectra of the N-DMBI-Ox-doped SWCNT sheet that produced a Seebeck coefficient of 7.52 μVK^{-1} without UV irradiation (Fig. 3b). Interestingly, absorption due to $DMBI^+$ was not observed in the

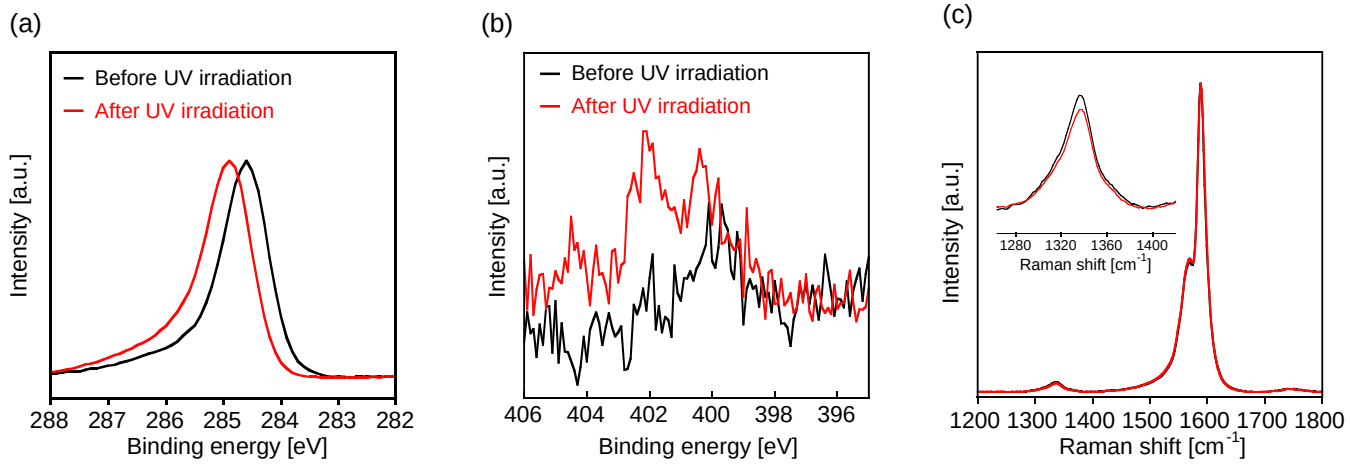

Fig. 4 XPS narrow scans of the (a) C 1s and (b) N 1s of a pristine SWCNT sheet (black line) and irradiated SWCNT sheet (red line). (c) Raman spectra of a non-doped SWCNT sheet (black line) and irradiated SWCNT sheet (red line).

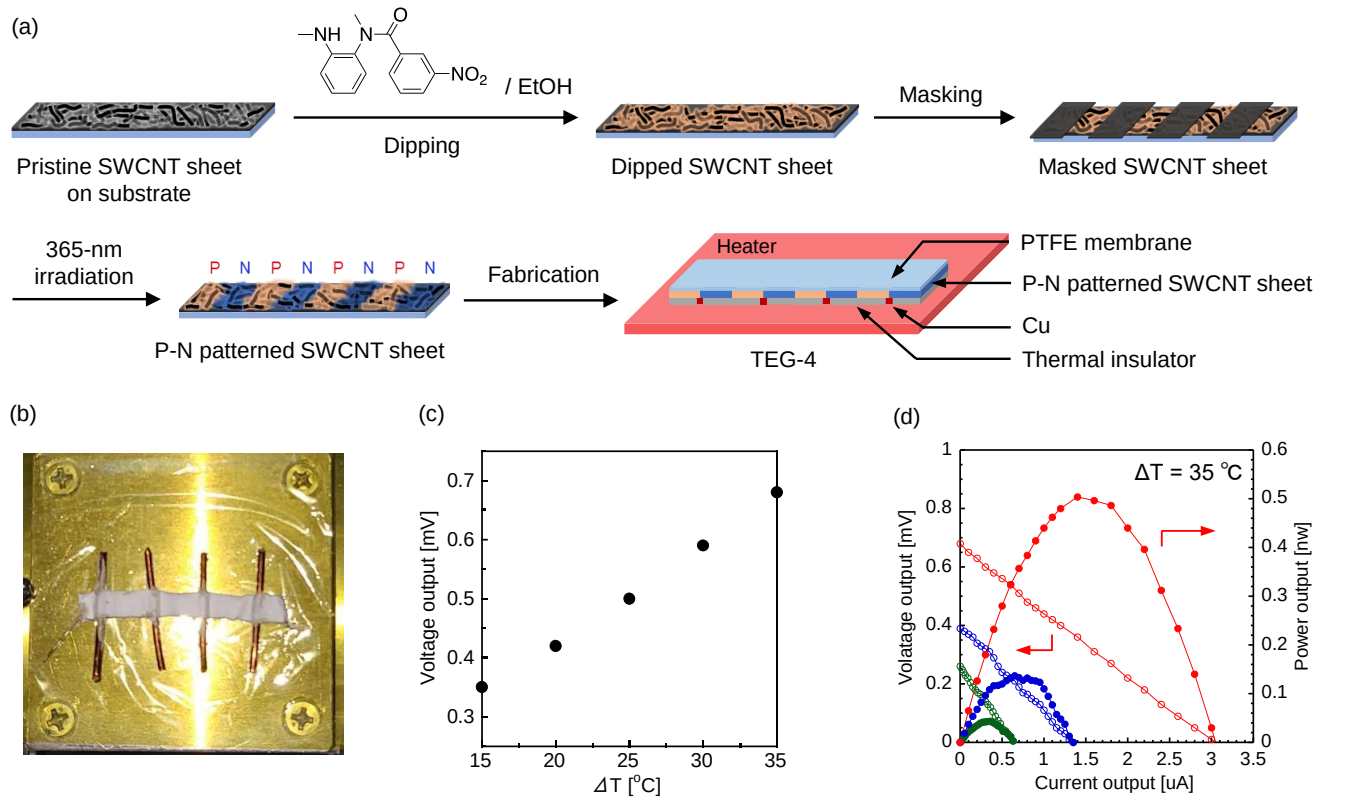

Fig. 5 (a) Schematic of the TEG fabrication process using p–n patterning of SWCNT sheets based on photoinduced doping of NO_2-DMBI-Ox. (b) Top view photograph of TEG-4 (dimensions: 4.0 × 40 mm). (c) Plot of the OCV of TEG-4 as a function of the difference temperature (ΔT). ΔT was defined as the difference between heater temperature and room temperature. (d) Voltage output (open circles) and power output (filled circle) of TEG-1 (green), TEG-2 (blue), and TEG-4 (red) as a function of the current output at a temperature difference of 35 °C.

extracted solution (Fig. S8†). We consider that electron doping without UV irradiation occurred via thermally activated electron transfer from N-DMBI-Ox to the SWCNTs during the dipping process. The different doping behaviors without irradiation between N-DMBI-Ox and NO_2-DMBI-Ox might be due to the difference in the redox potential of DMBI-Ox due to the substituent effect. Our previous study showed that N-DMBI has a greater doping capacity than NO_2-DMBI.[25] The photochemical doping capability of N-DMBI-Ox was confirmed by 365-nm irradiation of the N-DMBI-Ox-doped SWCNT sheets (Fig. S9†).

3.4 Surface Analysis of N-doped SWCNTs

X-ray photoelectron spectroscopy (XPS) was performed to evaluate the electronic state of the SWCNTs and confirm the chemical structure of the dopants on the SWCNTs. In the C 1s region, the dipped SWCNT sheet after 365-nm irradiation showed a peak shift from 284.6 eV to 285.0 eV compared with that of the pristine SWCNT sheet (Fig. 4a), supporting the n-doping of the SWCNTs. In the N 1s region, a broad peak centered at 400 eV, which was attributed to the imidazole moiety and nitro group on the phenyl ring, was observed before the photoinduced doping of the SWCNT sheet (black line in Fig. 4b). After irradiation, a new peak appeared at 402 eV, which was assigned to the nitrogen cation (red line in Fig. 4b). These results indicated the formation of NO_2-$DMBI^+$ and electron injection into the SWCNTs induced by UV irradiation. Fig. 4c shows the Raman spectra of the SWCNT sheets before and after photoinduced doping for 10 min. The intensity of the D-band at 1336 cm^{-1} originating from the sp^3 defects of SWCNTs was comparable to that of pristine SWCNTs, thus indicating that sp^3 defects did not form after photoinduced doping.

The thickness dependence of the photoinduced electron doping revealed that the photoinduced doping was effective up to 3 μm in the sheet thickness due to the limitation of the light penetration in the sheets (Fig. S10†). This is the first report of p- to n-type switching of SWCNTs using photochemical reactions of dopants. The photoinduced doping of CNT reported thus far is mostly n- to p-type switching based on the photolysis of the dopants, which requires prolonged light irradiation.[53] The present approach is advantageous because of the faster reaction.

The n-doped SWCNT sheet has been reported to be unstable under atmospheric conditions, which is likely due to oxidation by air in the absence of a stable counter cation.[54] To study the air stability of the doped SWCNT sheets, the Seebeck coefficient of the SWCNT sheet after 10 min of irradiation was monitored for 20 days (Fig. S11†). The absolute value of Seebeck coefficient gradually increased and finally reached zero after 20 days. Based on the recent reports demonstrating excellent air-stability lasting over several month,[25,48,55-59] we can expect that further optimization of the coverage of the SWCNT surface or the modification of the molecular structure will lead the improving of the air stability.

3.5 Fabrication of Planar SWCNT-based TEGs

By taking advantage of photoinduced doping, photo-patterning of the p-type SWCNTs into alternating p- and n-type regions using a photomask was carried out. The obtained p–n-patterned SWCNT sheets was then utilized for planar-type TEGs, as proposed by our group (Fig. 5a).[24] In planar-type SWCNT-based TEGs, electricity can be generated from a temperature gradient in the in-plane direction, in which the heat is injected in between p- and n-type region through thermal conductors, as illustrated in Fig. 5a. Thus, we prepared SWCNT sheets with one, two, and four p–n sequences by photoinduced doping using NO_2-DMBI-Ox as the dopant, and then Cu wires were attached as a thermal conductor capable of passivating the other area by a silica aerogel/poly(vinyl alcohol) composite as a thermal insulator (Fig. 5b).[60] SWCNT-based TEGs having one, two, and four p–n sequences were denoted as TEG-1, TEG-2, and TEG-4, respectively. Fig. 5c shows the open-circuit voltage (OCV) of TEG-4 placed on the hot plate in the room controlled at 25 °C. The OCV linearly increased as the temperature of the hot plate temperature increased, thus clearly indicating that the voltage was created by the Seebeck effect. Based on the open circuit voltage (OCV), we can estimate the in-plane temperature difference (ΔT') supplied in the device as $V = n(S_P–S_N)\Delta T'$, where V, n, S_P, and S_N are the OCV, number of p-n pattern units, P-type Seebeck coefficient [μV/K] and N-type Seebeck coefficient [μV/K]. Based on the equation, ΔT' of TEG-1, TEG-2, and TEG-4 were 3.1 °C, 2.3 °C, and 2.0 °C, respectively, which indicate the part of the temperature difference between the top and bottom of the sheet (ΔT = 35 °C) was utilized. Lower ΔT' for larger p-n patterns suggests that the large thermal conductivity of the SWCNT sheets in the in-plane direction results in the decrease of the ΔT'. At this stage, an effect of PTFE for ΔT' is not clear and a simulation study will be necessary to clarify the effects.

Fig. 5d shows the plots of the voltage output and power output profiles of TEG-1, TEG-2, and TEG-4 as a function of the current output placed on a hot plate (ΔT = 35 °C). We observed that the OCV and the maximum power density increased as the number of patterns increased and the power output reached a maximum of 0.504 nW (Fig. 5d). Compared with the fabrication of SWCNT patterning sheets by drop casting or vapor deposition of the dopants, the photoinduced doping method will offer p–n-patterned SWCNT sheets with high patterning resolution because diffusion of the dopants can be avoided.

4. Conclusion

We found a new photochemical reaction of DMBI-Ox that can form $DMBI^+$ in polar solvents as well as in the solid state based on UV absorption and ^1H NMR spectroscopy. UV-triggered intramolecular cyclization via δ-hydrogen transfer and then the elimination of hydroxyl ions may be the mechanism underlying the reaction. By exploiting the generation of hydroxyl ions, we successfully demonstrated the photoinduced electron doping of SWCNT sheets using NO_2-DMBI-Ox as the photoactive dopant. This doping method offers a facile preparation method for p–n-patterned SWCNT sheets using photo masks, and we successfully fabricated planar-type TEG devices using the p–n-patterned SWCNT sheet by placing the fabricated TEG device with four p–n sequences onto a hot plate (ΔT = 35 °C). An OCV and a maximum power density of 0.68 mV and 0.504 nW were obtained, respectively. We believe that this new photochemical reaction will offer various applications via n-doping of semiconducting materials.

Author Contributions

N.T. and T.F. designed the study and wrote the manuscript. N.T. and T.I. performed the experiments. T.I., I.Y., and A.H. analyzed the results and contributed to the discussion of the manuscript. All the authors discussed the results and revised the manuscript.

Conflicts of interest

There are no conflicts to declare.

Acknowledgements

This work was supported by KAKENHI (No. 18H01816, 19K23633, and 20K15355) and bilateral programs (No. AJ190078) of the Japan Society for the Promotion of Science (JSPS) and the Nanotechnology Platform Project from the Ministry of Education, Culture, Sports, Science, and Technology (MEXT), Japan, and Core Research for Evolutional Science and Technology (CREST) (No. AJ199002), and ACT-X (No. JPMJAX21KB) from the Japan Science and Technology Agency (JST), and The Thermal and Electric Energy Technology (TEET) Foundation.

Notes and references

1 W.-Y. Chen, X.-L. Shi, J. Zou, and Z.-G. Chen, *Mater. Sci. Eng. R Rep*. 2022, **151**, 100700.
2 M. Dargusch, W.-D. Li and Z.-G. Chen, *Adv. Sci.* 2020, **7**, 2001362.
3 M. Mukaida, K. Kirihara, S. Horike, and Q. Wei, *J. Mater. Chem. A* 2020, **8**, 22544-22556.
4 D.-Z. Wang, W.-D. Liu, M. Li, L.-C. Yin, H. Gao, Q. Sun, H. Wu, Y. Wang, X.-L. Shi, X. Yang, Q. Liu, and Z.-G. *Chen, Chem. Eng. J.* 2022, **441**, 136131.
5 S. Jhulki, H.-I. Un, Y.-F. Ding, C. Risko, S. K. Mohapatra, J. Pei, S. Barlow and S. R. Marder, *Chem* 2021, **7**, 1050-1065.
6 X. Yan, M. Xiong, J.-T. Li, S. Zhang, Z. Ahmad, Y. Lu, Z.-Y. Wang, Z.-F. Yao, J.-Y. Wang and X. Gu, *J. Am. Chem. Soc.* 2019, **141**, 20215-20221.
7 H. I. Un, S. A. Gregory, S. K. Mohapatra, M. Xiong, E. Longhi, Y. Lu, S. Rigin, S. Jhulki, C.-Y. Yang, T. V. Timofeeva, J.-Y. Wang, S. K. Yee, S. Barlow, S. R. Marder and J. Pei, *Adv. Energy Mater.* 2019, **9**, 1900817.
8 Y. Lu, Z.-D. Yu, R.-Z. Zhang, Z.-F. Yao, H.-Y. You, L. Jiang, H.-I. Un, B.-W. Dong, M. Xiong, J.-Y. Wang and J. Pei, *Angew. Chemie* 2019, **131**, 11512-11516.
9 Y. Shin, M. Massetti, H. Komber, T. Biskup, D. Nava, G. Lanzani, M. Caironi and M. Sommer, *Adv, Electron. Mater.* 2018, **4**, 1700581.
10 Y. Guo, W. Sato, K. Inoue, W. Zhang, G. Yu, E. Nakamura, *J. Mater. Chem. A* 2016, **4**, 18852-18856.
11 K. Shi, F. Zhang, C.-A. Di, T.-W. Yan, Y. Zou, X. Zhou, D. Zhu, J.-Y. Wang and J. Pei, *J. Am. Chem. Soc.* 2015, **137**, 6979-6982.

12 R. A. Schlitz, F. G. Brunetti, A. M. Glaudell, P. L. Miller, M. A. Brady, C. J. Takacs, C. J. Hawker and M. L. Chabinyc, *Adv. Mater.* 2014, **26**, 2825-2830.
13 B. D. Naab, S. Himmelberger, Y. Diao, K. Vandewal, P. Wei, B. Lussem, A. Salleo and Z. Bao, *Adv. Mater.* 2013, **25**, 4663-4667.
14 M. Lu, H. T. Nicolai, G.-J. A. H. Wetzelaer and P. W. M. Blom, *Appl. Phys. Lett.* 2011, **99**, 173302.
15 J. Liu, S. Maity, N. Roosloot, X. Qiu, L. Qiu, R. C. Chiechi, J. C. Hummelen, E. von Hauff and L. J. A. Koster, *Adv. Electron. Mater*. 2019, **5**, 1800959.
16 Q. Bao, X. Liu, S. Braun, Y. Li, J. Tang, C. Duan and M. Fahlman, *ACS Appl. Mater. Interfaces* 2017, **9**, 35476-35482.
17 S. Rossbauer, C. Müller and T. D. Anthopoulos, *Adv. Funct. Mater.* 2014, **24**, 7116-7124.
18 P. Wei, J. H. Oh, G. Dong and Z. Bao, *J. Am. Chem. Soc.* 2010, **132**, 8852-8853.
19 S.-J. Kwon, T.-H. Han, Y.-H. Kim, T. Ahmed, H.-K. Seo, H. Kim, D. J. Kim, W. Xu, B. H. Hong, J.-X. Zhu and T.-W. Lee, *ACS Appl. Mater. Interfaces* 2018, **10**, 4874-4881.
20 W. Xu, T.-S. Lim, H.-K. Seo, S.-Y. Min, H. Cho, M.-H. Park, Y.-H. Kim and T.-W. Lee, *Small* 2014, **10**, 1999-2005.
21 N. Liu, H. Tian, G. Schwartz, J. B.-H. Tok, T.-L. Ren and Z. Bao, *Nano Lett.* 2014, **14**, 3702-3708.
22 P. Wei, N. Liu, H. R. Lee, E. Adijanto, L. Ci, B. D. Naab, J. Q. Zhong, J. Park, W. Chen, Y. Cui and Z. Bao, *Nano Lett.* 2013, **13**, 1890-1897.
23 Y. Wang, Q. Li, J. Wang, Z. Li, K. Li, X. Dai, J. Pan and H. Wang, *Nano Energy* 2022, **93**, 106804.
24 R. Yamaguchi, T. Ishii, M. Matsumoto, A. Borah, N. Tanaka, K. Oda, M. Tomita, T. Watanabe and T. Fujigaya, *J. Mater. Chem. A* 2021, **9**, 12188-12195.
25 Y. Nakashima, R. Yamaguchi, F. Toshimitsu, M. Matsumoto, A. Borah, A. Staykov, M. S. Islam, S. Hayami and T. Fujigaya, *ACS Appl. Nano Mater.* 2019, **2**, 4703-4710.
26 Y. Nakashima, N. Nakashima and T. Fujigaya, *Synthetic Metals* 2017, **225**, 76-80.
27 S. Zhang, B. D. Naab, E. V. Jucov, S. Parkin, E. G. B. Evans, G. L. Millhauser, T.V. Timofeeva, C. Risko, J.-L. Brédas, Z. Bao, S. Barlow and S. R. Marder, *Chem. Eur. J.* 2015, **21**, 10878-10885.
28 O. Bardagot, C. Aumaître, A. Monmagnon, J. Pécaut, P.-A. Bayle and R. Demadrille, *Appl. Phys. Lett.* 2021, **118**, 203904.
29 J. Yu and M. Lu, *Res. Chem. Intermed*. 2015, **41**, 10017−10025.
30 X. Sun, X.-H. Lv, L.-M. Ye, Y. Hu, Y.-Y. Chen, X.-J. Zhang, and M. Yan, *Org. Biomol. Chem.* 2015, **13**, 7381−7383.
31 J. Yu and M. Lu, *Synth. Commun.* 2015, **45**, 2148−2157.
32 T. B. Nguyen, J. L. Bescont, L. Ermolenko and A. Al-Mourabit, *Org. Lett.* 2013, **15**, 6218−6221.
33 H. G. F. Richter, G. M. Benson, D. Blum, E. Chaput, S. Feng, C. Gardes, U. Grether, P. Hartman, B. Kuhn, R. E. Martin, J.-M. Plancher, M. G. Rudolph, F. Schuler, S. Taylor and K. H. Bleicher, *Bioorganic Med. Chem. Lett.* 2011, **21**, 191–194.
34 C.-S. Cho and J.-U. Kim, *Bull. Korean Chem. Soc.* 2008, **29**, 1097−1098.
35 F. M. Rivas, U. Riaz, A. Giessert, J. A. Smulik and S. T. Diver, *Org. Lett*. 2001, **3**, 2673-2676.
36 A. J. Kell, D. L. B. Stringle and M. S. Workentin, *Org. Lett*. 2000, **2**, 3381–3384.
37 A. Osuka, H. Shimizu, H. Suzuki and K. Maruyama, *Chem. Lett.* 1987, **16**, 1061-1064.
38 S. Ariel, V. Ramamurthy, J. R. Scheffer and J. Trotter, *J. Am. Chem. Soc.* 1983, **105**, 6959-6960.
39 A. Osuka, *J. Org. Chem.* 1982, **47**, 3131-3139.
40 P. J. Wagner, K.-C. Liu and Y. Noguchi, *J. Am. Chem. Soc.* 1981, **103**, 3837-3841.
41 R. G. W. Norrish and C. H. Bamford, *Nature* 1937, **140**, 195-196.
42 R. G. W. Norrish and C. H. Bamford, *Nature* 1936, **138**, 1016.
43 R. G. W. Norrish and M. E. S. Appleyard, *J. Chem. Soc. (Resumed)* 1934, 874-880.
44 F. Pallini, S. Mattiello, M. Cassinelli, P. Rossi, S. Mecca, W. L. Tan, M. Sassi, G. Lanzani, C. R. McNeill, M. Caironi and L. Beverina, *ACS Appl. Energy Mater.* 2022, **5**, 2421-2429.
45 G. Stewart, K. Smith, A. Chornes, T. Harris, T. Honeysucker and H. Yu, *Environ. Chem. Lett.* 2010, **8**, 301-306.
46 B. Chen, C. Yang and N. K. Goh, *J. Environ. Sci.* 2006, **18**, 1061-1064.
47 M. Yamada, C. Goto, H. Aoki, Y. Nonoguchi and T. Kawai, *J. Mater. Chem. A*, 2020, **8**, 22969–22973.
48 Y. Nonoguchi, M. Nakano, T. Murayama, H. Hagino, S. Hama, K. Miyazaki, R. Matsubara, M. Nakamura and T. Kawai, *Adv. Funct. Mater.* 2016, **26**, 3021-3028.
49 W. Zhou, Q. Fan, Q. Zhang, L. Cai, K. Li, X. Gu, F. Yang, N. Zhang, Y. Wang, H. Liu, W. Zhou, and S. Xie, *Nat. Commun.* 2017, **8**, 14886.
50 X. Dai, Y. Wang, K. Li, G. Li, J. Wang, X. Sun, L. Zhang, and H. Wang, *ACS Energy Lett.* 2021, **6**, 4355-4364.
51 J. L. Bitter, J. Yang, S. Beigzadeh Milani, C. T. Jafvert and D. H. Fairbrother, *Environ. Sci. Nano*. 2014, **1**, 324-337.
52 B. Angana, W. Huang, T. Ishii, R. Yamaguchi, E. Honjo, N. Tanaka, T. Fujigaya, *Jpn. J. Appl. Phys.* 2022, **61**,121004.
53 S. Horike, T. Fukushima, T. Saito, Y. Koshiba and K. Ishida, *Chem. Phys. Lett.* 2018, **691**, 219-223.
54 J. Hone, I. Ellwood, M. Muno, A. Mizel, M. L. Cohen, A. Zettl, A. G. Rinzler and R. Smalley, *Phys. Rev. Lett*. 1998, **80**, 1042.
55 Y. Nonoguchi, K. Ohashi, R. Kanazawa, K. Ashiba, K. Hata, T. Nakagawa, C. Adachi, T. Tanase, and T. Kawai *Sci. Rep*. 2013, **3**, 3344.
56 H. Wang, P. Wei, Y. Li, J. Han, H. R. Lee, B. D. Naab, N. Liu, C. Wang, E. Adijanto, B. C.-K. Tee, S. Morishita, Q. Li, Y. Gao, Y. Cui, and Z. Bao, *Proc Natl Acad Sci USA* 2014, **111**, 4776–4781.
57 T. Fukumaru, T. Fujigaya and N. Nakashima, *Sci. Rep.*, 2015, **5**, 7951.
58 Y. Nonoguchi, Y. Iihara, K. Ohashi, T. Murayama, and T. Kawai, *Chem. Asian J.* 2016, **11**, 2423–2427.
59 B. A. MacLeod, N. J. Stanton, I. E. Gould, D. Wesenberg, R. Ihly, Z. R. Owczarczyk, K. E. Hurst, C. S. Fewox, C. N. Folmar, K. Holman Hughes, B. L. Zink, J. L. Blackburn, A. J. Ferguson, *Energy Environ. Sci.* 2017, **10**, 2168–2179.
60 H. M. Kim, Y. J. Noh, J. Yu, S. Y. Kim and J. R. Youn, *Compos. Part A Appl. Sci. Manuf.* 2015, **75**, 39-45.

